To be published in Journal of Optical Communications and Networking:

Title: Performance analysis of atmospheric optical communication systems with spatial diversity affected by correlated turbulence

Authors: Antonio Jurado-Navas,María Álvarez-Roa,Carmen Álvarez-Roa,Francisco Fernández-Aragón,Thiago Raddo,Jose Maria Garrido-Balsells,Idelfonso Tafur Monroy

Accepted: 10 May 22

Posted 10 May 22

DOI: https://doi.org/10.1364/JOCN.452044

Performance analysis of atmospheric optical communication systems with spatial diversity affected by correlated turbulence

M. Álvarez-Roa[1], C. Álvarez-Roa[1], F. Fernández-Aragón[1], T. Raddo[2], J.M. Garrido-Balsells[1], I. Tafur-Monroy[3], and A. Jurado-Navas[1,*]

[1] Telecommunication Research Institute (TELMA), Universidad de Málaga, E.T.S. Ingeniería de Telecomunicación, Bulevar Louis Pasteur 35, 29010, Málaga (Spain)
[2] Engineering, Modeling & Applied Social Sciences Center, Federal University of ABC, Santo Andre, Brazil
[3] Institute for Photonic Integration, Eindhoven University of Technology, 5600 MB Eindhoven, The Netherlands
[*] Corresponding author: navas@ic.uma.es

Compiled April 20, 2022

This paper presents a complete analytical framework for obtaining the performance associated to a free-space optical (FSO) communication system with spatial diversity and equal gain-combining technique. The system is affected by gamma-gamma scintillations with different realistic degrees of channel correlation only depending on physical parameters of the link. We derive new analytical closed-form expressions for average bit error rate (ABER) considering different scenarios to provide a very realistic behavior of the system including different number of FSO receivers in several geometric configurations, with different receiving areas, different path lengths and a variety of turbulence conditions. Furthermore, a very accurate approximate closed-form expression is also derived for the ABER of any generic coding scheme with either a very complex or, directly, no closed-form expression for its associated conditional BER (CBER) that is firstly obtained in the ideal case of absence of turbulence. Numerical results via Monte-Carlo simulation are provided to corroborate the validity of all the derived analytical expressions.

http://dx.doi.org/10.1364/ao.XX.XXXXXX

1. INTRODUCTION

Free space optical (FSO) communications have been studied as a competitive solution for the establishment of wireless point-to-point links. This technology has become an attractive cost-effective solution to provide highly-secured and broadband transmissions in areas where fiber infrastructure is deficient or nonexistent [1–6]. In this respect, FSO communications benefit from its inherent huge unregulated bandwidth availability in optical frequencies, supporting the increasing traffic demand required by today's society. However, these systems can be affected by the atmospheric turbulence, characterized by a random space-time redistribution of the refractive index, and causing a variety of adverse effects on the propagating optical wave in regards to its temporal irradiance fluctuations, commonly described as scintillation [7]. That scintillation produces a turbulence-induced fading in the received signal intensity leading to a degradation of the overall system performance.

An appropriate solution to mitigate its degrading effects is to employ a spatial diversity reception [8–12]. In this technique, by using N apertures at the receiver side, the inherent redundancy of spatial diversity has the potential to significantly enhance the performance of FSO communication systems. A way to evaluate that performance is via knowledge of the analytical expression for the probability density function (pdf) of the sum of correlated irradiances seen at the receiver side. Thus, in [11], they proposed an analytical approach for the correlated gamma–gamma fading channel based on an $\alpha - \mu$ distribution. However, its parameters depend on nonlinear functions requiring numerical methods to be solved. In order to overcome that issue, Djordjevic et al. [12] calculated the multivariate constant correlated gamma-gamma distribution assuming that the correlation among small-scale turbulence eddies is neglected. The result is a pdf involving an infinite summation that may complicate the evaluation of further analytical expressions associated to the performance of the FSO system. Hence, in [13], new analytical closed-form ex-

pressions were derived for the pdf of the sum of identically distributed correlated gamma-gamma random variables leading to a mathematically tractable method to characterize the statistical behavior of the received optical irradiance in a spatial diversity context. To this aim, and in order to achieve compact expressions, it was assumed that the signals reaching the N receivers are deflected by the same eddies and, therefore, large scale effects are common for all of them. Accordingly, the existence of a certain degree of correlation between any pair of optical signals in the receiver side will be only owing to their associated small-scale scintillations. This feature is now studied in this paper, evaluating its impact on the overall system performance. To include realistic scenarios, the correlation factor is written in terms of the spatial coherence radius and so, all the results will only depend on physical parameters of the link. Furthermore, various physical receiver topologies are considered, analyzing their performance in terms of error probability and for different turbulence conditions. Thus, closed expressions are proposed for the average bit error rate (ABER) as a function of the channel coding scheme, the channel conditions and the level of correlation between detected signals. First, the on-off keying (OOK) case is analyzed for its simplicity and ease of implementation, to later compare its performance with the one obtained from the variable weight multiple pulse-position modulation (vw-MPPM) scheme, successfully proposed by the authors in indoor [14] and outdoor [15] wireless communications. That latter scheme was chosen as an illustrative example of any generic nonlinear block coding transmission technique whose conditional BER (CBER) cannot be derived in a closed-form expression. As a previous step, the hyperexponential curve fitting method presented in [16] is adopted to obtain a very accurate analytical expression for the ABER associated to that vw-MPPM technique. Finally, all the analytical results derived here were numerically validated by Monte-Carlo simulations.

It is worth mentioning that a terrestrial FSO link which consists of a single-mode semiconductor laser as the transmitter and N photodetectors as the receiver is considered, assuming an intensity modulation with direct detection (IM/DD) scheme and an equal gain combining (EGC) technique. Point receivers are supposed for which maximum adverse effects are observed.

2. SPATIAL DIVERSITY RECEPTION

Intensity fluctuations in the received signal due to channel fading induced by atmospheric turbulence can result in a considerable degradation of system performance. Spatial diversity techniques provide an attractive alternative approach for fading compensation with their inherent redundancy. This technology can be used over FSO links, which implies the deployment of multiple small aperture laser transmitters and receivers. To extract the maximum benefit from the spatial diversity technique, the spacing between receivers should be greater than the fading correlation length, which may be difficult to achieve in practice due to the limited available physical space or because the receiver spacing required for uncorrelated fading may exceed the beam diameter in power-limited links with well-collimated beams. In fact, the degree of correlation among the FSO receivers proved to be one of the main performance limiting factor of the system. Therefore we consider in this work how correlation among the different atmospheric scintillation sequences captured by each photodetector is affecting the overall performance when they are forming several geometric configurations inside a same magnitude of total receiving area.

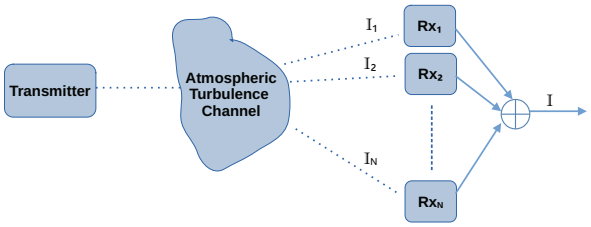

Fig. 1. Single-Input-Multiple-Output (SIMO) model for FSO systems with a laser transmitter and N optical receivers. The model will be representative to evaluate the impact of the spatial correlation between scintillation sequences.

A. System model

Figure 1 describes our single-input-multiple-output (SIMO) system model with spatial diversity reception considering N identical photodetectors and IM/DD modulation and detection technique. Thus, assuming EGC, the received optical irradiance, I, can be expressed as a sum of each individual $i-$th received irradiance by every single receiver aperture, which is a random variable with gamma-gamma distribution. This variable is the result of a modulation process that can be written as $I_i = X_i Y_i$, where X_i and Y_i are the random variables of the large-scale and small-scale scintillation-component respectively, corresponding to each photodetector.

It is assumed that the same large eddies affect the signal received by the N receiver apertures (see Appendix for a complete discussion on this assumption). Hence, the large-scale scintillation-component is a common contribution for all of them, i.e., $X_i = X, \forall i = 1 \dots N$, with X following a gamma distribution with shape parameters α_x and β_x=$1/\alpha_x$, denoted as $\mathcal{G}(\alpha_x, 1/\alpha_x)$. Note that, with this assumption, we consider the most unfavorable scenario for large-scale correlation, useful as a benchmark in optical systems design. In contrast, the diffractive small-scale turbulence effect Y_i depends on each aperture, although it is assumed that each Y_i is identically gamma-distributed and characterized by $\alpha_{Y_i} = \alpha$ and $\beta_{Y_i} = 1/(N\alpha)$, thus Y_i denoted as $\mathcal{G}(\alpha, 1/(N\alpha))$, as detailed in [13].

Note that α_x and α are related to the effective number of large-scale and small-scale turbulent cells, respectively, and their ranges vary from values very close to 1, for strong turbulence conditions, to values $>> 1$, for weak turbulence regimes [7]. As normalized irradiance is considered, $E[I] = 1$, then

$$I = X \sum_{i=1}^{N} Y_i = XV \tag{1}$$

where $V = \sum_{i=1}^{N} Y_i$, with V being a random variable describing the small-scale atmospheric effect over the combined received optical irradiance.

When taking into account the correlation factor between any pair of received small scale sequences, i.e. the correlation between the variables Y_i and Y_j with $i, j = 1 \dots N$, then we can build the corresponding real symmetric $N \times N$ correlation matrix, $\mathbf{C_y}$, given as:

$$\mathbf{C_y} = \begin{pmatrix} 1 & p_{12} & \cdots & p_{1N} \\ p_{21} & 1 & \cdots & p_{2N} \\ \vdots & \vdots & \ddots & \vdots \\ p_{N1} & p_{N2} & \cdots & 1 \end{pmatrix}_{N \times N} \tag{2}$$

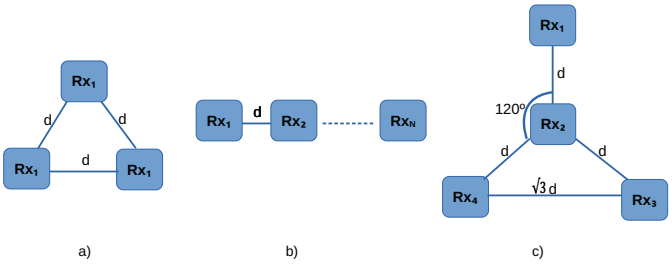

Fig. 2. Constant, exponential and star correlation models, a), b) and c), respectively, used for the simulations carried out.

with p_{ij} being the cross-correlation coefficient associated to the distance between the receivers at the positions i and j, respectively. Futher details can be found at [13].

B. Receiver distribution topologies

The space distribution of the receivers determines a particular geometry that may affect the performance of the system. Namely, we focus on three different spatial geometries of receivers that are depicted in Fig. 2: constant, exponential and star topologies.

The first one is the constant correlation model, described in [17], and associated to a configuration of evenly spaced receivers where $p_{ij} = p, \forall i, j = 1 \dots N$, with p representing the correlation coefficient between the gamma distributed signals received at adjacent photodetectors. Its most representative example corresponds to three receivers, $N = 3$, placed in an equilateral triangle, whose associated correlation matrix is described as

$$\mathbf{C_y} = \begin{pmatrix} 1 & p & p \\ p & 1 & p \\ p & p & 1 \end{pmatrix}_{3\times 3}. \quad (3)$$

On the other side, the second considered geometry, the exponential correlation model, corresponds to a lineal equidistant photodetectors array, [17], with the following correlation matrix

$$\mathbf{C_y} = \begin{pmatrix} 1 & p_1 & p_2 & p_3 & \dots & p_N \\ p_1 & 1 & p_1 & p_2 & \dots & p_{N-1} \\ p_2 & p_1 & 1 & p_1 & \dots & p_{N-2} \\ \dots & \dots & \dots & \dots & \dots & \dots \\ p_N & p_{N-1} & p_{N-2} & p_{N-3} & \dots & 1 \end{pmatrix}_{N\times N}. \quad (4)$$

Finally, we also consider a model of $N = 4$ receivers placed in what we call a star topology due to its physical shape, resembling a star [18, 19]; where there is a central photodetector surrounded by other three forming an angle of 120° between them with regard to that central photodetector. Its associated matrix is given by

$$\mathbf{C_y} = \begin{pmatrix} 1 & p_1 & p_2 & p_2 \\ p_1 & 1 & p_1 & p_1 \\ p_2 & p_1 & 1 & p_2 \\ p_2 & p_1 & p_2 & 1 \end{pmatrix}_{4\times 4}, \quad (5)$$

where the correlation factors, p_1 and p_2, are associated to a separation distance d and $\sqrt{3}d$, respectively, between adjacent photodetectors, as shown in Fig. 2c after using the law of sines.

C. Correlated channels

As detailed in previous sections, the correlation matrix describes the degree of dependence among channels in reception, which is defined in a straightforward manner by the correlation coefficient. From Eq. (1), such the correlation coefficient is obtained from the small-scale scintillation-component since the large-scale scintillation-component is a common contribution for all of the N receiver apertures.

Let us define now the correlation length ρ_c of irradiance fluctuations as the width of the irradiance covariance function at $1/e^2$ of its peak value. In other words, the correlation length describes the average speckle size at the receiver. This parameter is particularly useful in determining the size of the receiver aperture needed to mitigate the effect of atmospheric turbulence, mainly in strong turbulence. Note that ρ_c depends on both the weather and the link distance. For small-scale scintillations (the ones contributing to the correlation matrix, according to Eq. (1)), and following [20], the correlation length is determined by a) the Fresnel zone $\sqrt{L/k}$ under weak turbulence, with $k = 2\pi/\lambda$ being the wave number of optical radiation, with λ being the optical wavelength, and with L denoting the propagation path length; and b) by the spatial coherence radius ρ_0 (which is now smaller than the Fresnel zone) under strong turbulence. Note that, at the onset of strong fluctuations, the coherence radius approaches the size of the Fresnel zone. In this way, when the refractive index structure parameter C_n^2 is treated as constant, i.e., a horizontal FSO link, the plane wave spatial coherence radius ρ_0 is defined, from [20], as

$$\rho_0 = (1.46 C_n^2 k^2 L)^{-3/5}, \quad l_0 << \sqrt{\lambda L} << L_0, \quad (6)$$

where C_n^2 represents a measure of the strength of the turbulence at each moment, and L is the propagation path length.

So, summarizing, in this paper we consider

$$\rho_c = \begin{cases} \sqrt{L/k}, & \text{weak fluctuations} \\ (1.46 C_n^2 k^2 L)^{-3/5}, & \text{strong fluctuations} \end{cases} \quad (7)$$

Interestingly, Figure 3 shows the values of ρ_0 for different values of L, and for weak ($C_n^2 = 4 \times 10^{-15}$), moderate ($C_n^2 = 10^{-14}$) and strong ($C_n^2 = 10^{-13}$) turbulence conditions, assuming a wavelength of $\lambda = 1550$ nm. The performance of $\sqrt{L/k}$ is also provided. From that Fig. 3, we can observe that the stronger the intensity of turbulence, the lower the correlation factor among channels when short link distances are considered. In this respect, separations between receivers of solely a few centimeters are sufficient enough to have totally independent channels. On the contrary, when turbulence strength decreases, either photodetectors must be placed farther apart from the others or longer propagation path links are required to obtain the maximum benefit from the spatial diversity technique.

Moreover, and from [21, 22], we adopt a more restrictive value for the Fresnel zone size: $\sqrt{\lambda L}$. Hence, and with the aim of obtaining the maximum performance from a spatial diversity technique, the receivers will have to be separated by a distance greater than or equal to ρ_c.

Now that aforementioned spatial correlation length given in Eq. (7) can be applied to calculate the cross-correlation coefficients in the correlation matrix by using the covariance function. In [21, 23], a Gaussian spatial covariance function for the log-amplitude fluctuations is employed that approximates the theoretical one resulting from Rytov theory [22]. This technique is widely used in line-of-sight propagation problems because it

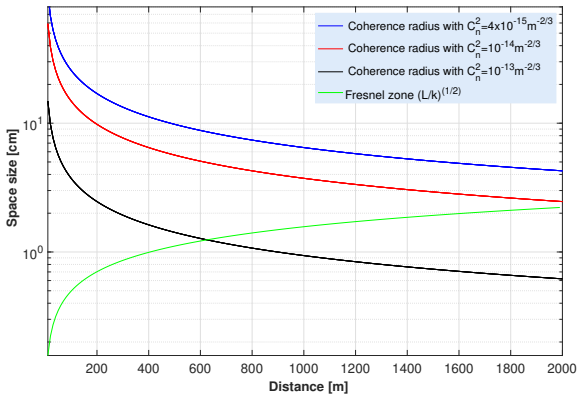

Fig. 3. Spatial coherence radius value, ρ_0, dependent on the length of the optical channel, L, for $C_n^2 = 4 \times 10^{-15}$ (blue line), $C_n^2 = 10^{-14}$ (red line) y $C_n^2 = 10^{-13}$ (black line), related to conditions of weak, moderate and strong turbulence, respectively.

simplifies the procedure of obtaining both amplitude and phase fluctuations and was extended to any regime of turbulence via the modified Rytov theory [20].

On another note, a useful property in turbulent media is the well-known Taylor's hypothesis of frozen turbulence [22, 24]. Under this hypothesis, the collection of atmospheric eddies will remain frozen in relation to one another, while the entire set is transported as a whole along some direction by the wind. When a narrow beam propagating over a long distance is assumed, the refractive index fluctuations along the direction of propagation are well-averaged and are weaker than those along the transverse direction to propagation. Hence, based on the Taylor's frozen turbulence hypothesis, spatial statistics can be converted to temporal statistics by knowledge of the average wind speed transverse to the direction of propagation, $u_\perp$ [22, 24], Thus by using both the Gaussian spatial covariance function and the space-to-time conversion of statistics provided by the frozen turbulence hypothesis, the covariance function $B_I(\rho, L)$ for the irradiance fluctuations can be written as

$$B_I(u_\perp \tau, L) = B_I(\rho, L) = B_I(d_{ij}, L) = \sigma_I^2 \exp\left(-\frac{d_{ij}^2}{\rho_c^2}\right), \quad \textbf{(8)}$$

where d_{ij} is the separation distance between positions i and j in the plane of the receiver, perpendicular to the direction of propagation. From Eq. (8), the normalized covariance function is defined as

$$b_I(d_{ij}) = \frac{B_I(d_{ij})}{\sigma_I^2} = \rho_{I_{ij}}. \quad \textbf{(9)}$$

Thus we can obtain a normalized correlation matrix for irradiance fluctuations for N receivers in a plane transverse to the direction of propagation of the light beam. Hence

$$\mathbf{C_I} = \begin{pmatrix} 1 & \rho_{I_{12}} & \cdots & \rho_{I_{1N}} \\ \rho_{I_{21}} & 1 & \cdots & \rho_{I_{2N}} \\ \cdots & \cdots & \cdots & \cdots \\ \rho_{I_{N1}} & \rho_{I_{N2}} & \cdots & 1 \end{pmatrix}_{NxN}. \quad \textbf{(10)}$$

To sum up, the correlation coefficient, ρ_I, for the irradiance fluctuation which will be valid for any turbulent condition, and will depend on both the separation distance between the N receivers, d_{ij}, and on the correlation length ρ_c as

$$\rho_{I_{ij}} = \exp\left(-\frac{d_{ij}^2}{\rho_c^2}\right). \quad \textbf{(11)}$$

To obtain the corresponding normalized covariance function for small scales, $\mathbf{C_y}$, we must calculate its correlation coefficients, $\rho_{Y_i,Y_j} = p_{i,j}$, following the notation provided in Eqs. (3)-(5). To this aim, we derive the correlation coefficient between I_i and I_j, both gamma-gamma random variables, in a straightforward manner thanks to the independence of the large- and small-scale fading coefficients, and assuming that the correlated random variables in Eq. (1) are combined with the EGC technique. Thus:

$$\rho_{I_{ij}} = \frac{B_{I_i,I_j}(d_{ij}, L)}{\sqrt{\sigma_{I_i}^2 \sigma_{I_j}^2}} = \frac{\rho_{Y_i,Y_j}\alpha_x + \rho_{X_i,X_j}\alpha + \rho_{Y_i,Y_j}\rho_{X_i,X_j}}{\alpha_x + \alpha + 1}. \quad \textbf{(12)}$$

where

$$\rho_{X_{ij}} = \frac{B_{X_i,X_j}(d_{ij}, L)}{\sqrt{\sigma_{X_i}^2 \sigma_{X_j}^2}}; \quad \textbf{(13)}$$

$$\rho_{Y_{ij}} = \frac{B_{Y_i,Y_j}(d_{ij}, L)}{\sqrt{\sigma_{Y_i}^2 \sigma_{Y_j}^2}}. \quad \textbf{(14)}$$

Since large-scale effects are common for the N receivers, i.e. we assume that $X_i = X, \forall i = 1 \ldots N$, then $\rho_{X_{ij}} = 1$. Accordingly, as in [11], we can obtain ρ_{Y_i,Y_j} as

$$\rho_{Y_{ij}} = p_{i,j} = \frac{(\alpha_x + \alpha + 1)\rho_{I_{ij}} - \alpha}{\alpha_x + 1} \quad \textbf{(15)}$$

and now can be inserted in Eq. (2) to finally obtain $\mathbf{C_y}$.

To achieve the maximum benefit of the spatial diversity technique, the correlation coefficient must be close to 0, so the separation distance between receivers must be sufficient to consider channels as independent as possible.

D. Statistical distribution of the received irradiance I

The channel model assumed here is based on the modified Rytov theory, defining the normalized irradiance as a product of two gamma random processes related to the large- and small-scale turbulent eddies, respectively, Therefore, and from Eq. (1), the irradiance gamma-gamma pdf, $f_I(I)$, assumes that small scale irradiance fluctuations are modulated by large-scale irradiance fluctuations of the propagating wave. Then, the V pdf can be calculated in the way proposed in [25]. Next, the statistical distribution of the total received irradiance, I, can be directly obtained by averaging the pdf of V over the gamma distribution characterizing the variable X, obtaining, as shown in [13], the pdf of the combined received irradiance as

$$f_I(I) = \frac{2}{[\det(\mathbf{A})]^\alpha \Gamma(\alpha_x)} \sum_{i=1}^{N'} \sum_{m=1}^{\alpha_i} \frac{c_{mi}}{\Gamma(m)} \lambda_i^{\frac{m-\alpha_x}{2}} \alpha_x^{\frac{m+\alpha_x}{2}} \times I^{N\alpha - 1 - \frac{m-\alpha_x}{2}} K_{m-\alpha_x}\left(2\sqrt{\frac{\alpha_x I}{\lambda_i}}\right). \quad \textbf{(16)}$$

where $\{\lambda_i\}_{i=1}^N$ are the eigenvalues of the matrix $\mathbf{A} = \mathbf{DC}$, with $\mathbf{D}$ being a $N \times N$ diagonal matrix with entries β for $i = 1 \ldots N$, whereas $\mathbf{C} = \sqrt{\mathbf{C_y}}$ is a $N \times N$ positive definite correlation matrix whose elements are the correlation coefficients of the underlying Gaussian processes that lead to the gamma distributed

fading; and $\det(\mathbf{A}) = \prod_{i=1}^{N} \lambda_i$. Furthermore, $\Gamma(\cdot)$ corresponds to the gamma function, N' is the number of the different eigenvalues of matrix $\mathbf{A}$ and $K_\nu(\cdot)$ is the modified Bessel function of the second kind and order ν. On the other hand, The parameter α_i is the product of the algebraic multiplicity of the eigenvalue, denoted as $\mu_A(\lambda_i)$, with the parameter α, i.e. $\alpha_i = \mu_A(\lambda_i) \cdot \alpha$. It is obtained using the partial fraction expansion method described in [26] for performing the conversion from product to summation of fractions that is applied in [Eq. (22), 13] to obtain [Eq. (23), 13] . Finally, c_{mi} is a coefficient depending on I and arising from the partial fraction expansion procedure written as

$$\begin{aligned} c_{mi} =& \frac{1}{(\alpha_i - m)!} \frac{\mathrm{d}^{\alpha_i - m}}{\mathrm{d}w^{\alpha_i - m}} \left[\prod_{\substack{j=1 \\ j \neq i}}^{N'} \frac{1}{(w - d_j)^{\alpha_j}} \right]_{w = d_i} = \\ =& \frac{1}{(\alpha_i - m)!} \sum_{k_1 + \overset{\hat{i}}{\ldots} + k_{N'} = \alpha_i - m} \binom{\alpha_i - m}{k_1 \cdots \overset{\hat{i}}{\ldots} \cdots k_{N'}} \\ & \times \prod_{\substack{j=1 \\ j \neq i}}^{N'} \left[(-1)^{k_j} (\alpha_j)_{k_j} (d_i - d_j)^{-\alpha_j - k_j} \right], \end{aligned} \tag{17}$$

where $\hat{i}$ means that k_i is omitted in the previous corresponding sequences. Then $(\alpha_j)_{k_j}$ represents the Pochhammer symbol with $d_i = -I/\lambda_i$, α_i is the product of the algebraic multiplicity of the eigenvalue, denoted as $\mu_A(\lambda_i)$ and the set of k_i coefficients arises from the multinomial theorem.

Two particular scenarios can be considered from Eq. (16). The first one arises when the small-scale scintillation sequences,Y_i, are completely uncorrelated whereas the second one is obtained when those received sequences are totally correlated. For the first scenario, small-scale effects are considered completely independent and the correlation matrix, $\mathbf{C_Y}$, is reduced to a diagonal matrix. For this case, large and small scale effects are modeled as $X \sim \mathcal{G}(\alpha_x, \beta_x)$ and $V = \sum_{i=1}^{N} Y_i \sim \mathcal{G}(N\alpha, 1/(N\alpha))$, respectively. The second scenario consists of receiving N totally correlated small-scale irradiance fluctuations. Hence, $V = \sum_{i=1}^{N} Y_i \sim \mathcal{G}(\alpha, 1/(\alpha))$. Then, the irradiance pdf follows a classic gamma-gamma distribution [27]. In the next section, some analytical BER expressions will be derived in order to characterize the system performance under any turbulence regime, any number of photodetectors, any degree of correlation among their received sequences, and any coding technique for the three topologies shown in this Section, and representing any possible realistic scenario. Note that, in this paper, weather-induced attenuation has not been considered for the sake of clarity. Although that effect also degrades the performance of FSO systems in the way shown in [28], however, due to its deterministic nature, such atmospheric attenuation acts merely as a scaling factor as indicated in [29].

3. AVERAGE BER FOR UNCODING OOK TRANSMISSION SCHEME

Bit error rate (BER) is one of the most useful figures-of-merit to assess the performance of any communication link. In this section, we derive the BER expression assuming an IM/DD link using OOK affected by additive white Gaussian noise (AWGN) with zero mean and variance σ_n^2, owing to the high intensity shot noise produced by the ambient light. Afterward, in the next section, we will generalize this expression to any coded transmission scheme.

As a previous step, the associated conditional BER (CBER) is firstly calculated for a given electrical signal-to-noise ratio (SNR) when analyzing an AWGN channel in the ideal case of absence of turbulence (namely denoted by γ_0), assuming each transmitted symbol equally likely to be sent. Furthermore, the instantaneous electrical SNR can be defined as SNR$= i_S/\sigma_n = \sqrt{\gamma}$, with $i_S = RP_rI$ being the detector signal current and where σ_n designates the root-mean-square (rms) noise current. Accordingly, the electrical SNR in absence of atmospheric fluctuations is henceforth SNR$_0 = \sqrt{\gamma_0}$ and it is obtained as i_{S_0}/σ_n, with $i_{S_0} = RP_r$ representing the signal current in the ideal case of absence of turbulence, with $\gamma_0 = \frac{(P_rR)^2}{\sigma_n}$, and consequently, $\gamma = I^2\gamma_0$. Hence, and from [30], the CBER associated to an IM/DD AWGN channel using OOK is expressed as

$$\mathrm{CBER}(I, \gamma_0) = P_b(e|I) = \frac{1}{2}\mathrm{erfc}\left(\frac{P_rRI}{\sigma_n\sqrt{2}}\right) = \frac{1}{2}\mathrm{erfc}\left(I\sqrt{\frac{\gamma_0}{2}}\right), \tag{18}$$

where P_r is the average of total received optical power, with R being the responsivity and with σ_n^2 denoting the AWGN variance whereas erfc$(\cdot)$ is the complementary error function.

Now, as shown in [30], the ABER, $P_b(e)$, can be obtained by averaging $P_b(e|I)$ given in Eq. (18) over $f_I(I)$ given in Eq. (16):

$$P_b(e) = \int_0^\infty P_b(e|I) f_I(I) \mathrm{d}I. \tag{19}$$

To solve Eq. (19), we express both the Bessel function included in (16), $K_{a-b}(\cdot)$, and the complementary error function from Eq. (18), erfc$(\cdot)$, as Meijer-G functions using [Eqs. (07.34.03.0605.01) and (07.34.03.0619.01), 31], respectively. Thus:

$$G_{0,2}^{2,0}\left(z \middle| a, b\right) = 2z^{\frac{a+b}{2}} K_{a-b}\left(2\sqrt{z}\right); \tag{20}$$

$$G_{1,2}^{2,0}\left(z \middle| \begin{matrix} a \\ a-1, a-1/2 \end{matrix}\right) = \sqrt{\pi} z^{a-1} \mathrm{erfc}(\sqrt{z}). \tag{21}$$

Now we can solve Eq. (19) by applying Eq. (07.34.21.0013.01) from [31]. Hence

$$\begin{aligned} P_b(e) =& \frac{1}{4\pi^{3/2}[\det(\mathbf{A})]^{\alpha}\Gamma(\alpha_x)} \sum_{i=1}^{N'} \sum_{m=1}^{\alpha_i} \frac{1}{\Gamma(m)} \frac{\lambda_i^{\frac{m-\alpha_x}{2}} \alpha_x^{\frac{m+\alpha_x}{2}}}{(\alpha_i - m)!} \\ & \times \sum_{k_1 + \overset{\hat{i}}{\ldots} + k_{N'} = \alpha_i - m} \binom{\alpha_i - m}{k_1 \cdots \overset{\hat{i}}{\ldots} \cdots k_{N'}} 2^{2N\alpha - m + \alpha_x} \\ & \times 2^{\sum_{\substack{j=1 \\ j \neq i}}^{N'} [-2\alpha_j - 2k_j]} \\ & \times \prod_{\substack{j=1 \\ j \neq i}}^{N'} \left[(-1)^{k_j} (\alpha_j)_{k_j} \left(\frac{-1}{\lambda_i} + \frac{1}{\lambda_j} \right)^{-\alpha_j - k_j} \right] \\ & \times \left(\frac{\alpha_x}{\lambda_i} \right)^{-\left(N\alpha - \frac{m-\alpha_x}{2} + \sum_{\substack{j=i \\ j \neq i}}^{N'} [-\alpha_j - k_j]\right)} \\ & \times G_{5,2}^{2,4}\left(\frac{8\gamma_0\lambda_i^2}{\alpha_x^2} \middle| \begin{matrix} A, B, C, D, 1 \\ 0, \frac{1}{2} \end{matrix} \right), \end{aligned} \tag{22}$$

where

$$A=\frac{1+\sum_{\substack{j=1\\ j\neq i}}^{N'}[\alpha_j+k_j]-N\alpha}{2},\ C=\frac{1+\sum_{\substack{j=1\\ j\neq i}}^{N'}[\alpha_j+k_j]-N\alpha+m-\alpha_x}{2},$$
$$B=\frac{2+\sum_{\substack{j=1\\ j\neq i}}^{N'}[\alpha_j+k_j]-N\alpha}{2},\ D=\frac{2+\sum_{\substack{j=1\\ j\neq i}}^{N'}[\alpha_j+k_j]-N\alpha+m-\alpha_x}{2}.$$

From the latter equation, we can distinguish two particular scenarios associated to the two extreme cases of $p=0$ and $p=1$, corresponding to non-correlated (nc) and totally correlated (tc) small-scale scintillations. After some algebraic manipulations, Eq. (22) can be written, respectively, as

$$P_b^{nc}(e)=\frac{2^{N\alpha+\alpha_x-1}}{4\pi\sqrt{\pi}\Gamma(N\alpha)\Gamma(\alpha_x)}\times G_{5,2}^{2,4}\left(\frac{8\gamma_0}{(\alpha_x N\alpha)^2}\middle|\begin{matrix}\frac{1-N\alpha}{2},\frac{2-N\alpha}{2},\frac{1-\alpha_x}{2},\frac{2-\alpha_x}{2},1\\ 0,\frac{1}{2}\end{matrix}\right) \tag{23}$$

$$P_b^{tc}(e)=\frac{2^{\alpha+\alpha_x-1}}{4\pi\sqrt{\pi}\Gamma(\alpha)\Gamma(\alpha_x)}\times G_{5,2}^{2,4}\left(\frac{8\gamma_0}{(\alpha_x\alpha)^2}\middle|\begin{matrix}\frac{1-\alpha}{2},\frac{2-\alpha}{2},\frac{1-\alpha_x}{2},\frac{2-\alpha_x}{2},1\\ 0,\frac{1}{2}\end{matrix}\right). \tag{24}$$

4. AVERAGE BER FOR A GENERIC CODING TRANSMISSION SCHEME

Through this section, we want to show how to derive analytical closed-from expressions for the exact ABER of FSO systems with spatial diversity and correlated channels employing any generic coding scheme. As a representative example of that latter one, we analyze the use of vw-MPPM, successfully proposed by the authors in indoor [14] and outdoor [15] wireless communications due to its high efficiency.

The vw-MPPM scheme is seen as a type of modulation whose purpose is to increase the peak-to-average optical power ratio (PAOPR) parameter in order to provide better performance in the optical link. This is a desired feature for any FSO system affected by turbulence, overcoming the imposed distortion when a system bandwidth constraint is required. The basic design criterion is to keep the average optical power transmitted at a constant level.

On another note, rate-adaptive transmission schemes are usually preferred for keeping the quality of service against the adverse channel conditions. In this respect, and depending on the available SNR, the bit rate will be adapted (the stronger the intensity of turbulence, the slower the data rate) until a sufficiently low error probability is attained. Thus, the rate-adaptive transmission scheme using block coding of variable Hamming weight is a very good alternative to maximize the link performance, achieving a high rate adaptability by simply changing the coding translation matrix. This coding technique is based on multiple pulse-position modulation (MPPM) where codewords with different Hamming weights are allowed. This fact minimizes the presence of pulses at the optical signal leading to an increment in PAOPR so vw-MPPM can be seen as an improved version of both conventional classical scheme based on pulse-position modulation (PPM) and MPPM in terms of link performance.

For the sake of completeness, we briefly describe the vw-MPPM technique. Thus, the coding process consists of a translation procedure between the input data alphabet, C_K, with k-bit codewords, and the coded alphabet, $\widetilde{C}_N$, a subset of C_N, comprising 2^n possible n-bit codewords. For the proper choice of $\widetilde{C}_N$, codewords with different Hamming weight are proposed, leading to a block coding with a variable amount of pulses. Hence, if $C_{n,w}$ is the block code consisting of all possible codewords of length n with a Hamming weight of w, the code $\widetilde{C}_N$ is defined using the following codes $C_{n,w}$:

$$\widetilde{C}_N=\left(\bigcup_{i=0}^{x-1}C_{n,i}\right)\cup\widetilde{C}_{n,x}, \tag{25}$$

with $\widetilde{C}_{n,x}$ representing the codewords subset of $C_{n,x}$ used in $\widetilde{C}_N$. Thus, the coding table associated with $\widetilde{C}_N$ consists of all the possible codewords with Hamming weight i, $0\leq i\leq(x-1)$, together with a subset of x-weighted codewords given by the expression $2^k-\sum_{i=0}^{x-1}\binom{n}{i}$, where $\binom{n}{i}$ is the number of codewords of $C_{n,i}$. In this sense, the rate associated to the block code is given by k/n.

Since vw-MPPM is a nonlinear block coding scheme, the standard methods based on the characteristic functions of linear block codes are not suitable to obtain closed-form expressions of CBER. This is another reason why we have selected this modulation as a representative example of any generic coding technique. For them, the authors successfully proposed in [16] a novel alternative based on a hyperexponential fitting technique to achieve a very accurate CBER expression, given by

$$\mathrm{CBER}(I,\gamma_0)=P_b(e|I)\approx a\exp\left[-b\left(\gamma_0 I^2\right)^c\right] \tag{26}$$

with γ_0 being, again, the electrical SNR in absence of turbulence, and where the hyperexponential fitting parameters are $a,b,c\in\Re^+$. In Table 1 we show the hyperexponential fitting parameters for most relevant vw-MPPM code rates [14].

Code Rate	a	b	c
2/3	0.3870	2.7150	0.8890
6/12	0.6364	6.8958	0.8871
9/36	0.7246	42.4424	0.8600

Table 1. Hyperexponential fitting parameters a, b and c in absence of turbulence

Thus, the ABER, $P_b(e)$, is again obtained by averaging $P_b(e|I)$ given in (26) over $f_I(I)$ presented in Eq. (16), in the form:

$$P_b=\int_0^\infty a\exp\left[-b\left(\gamma_0 I^2\right)^c\right]f_I(I)dI. \tag{27}$$

Following a similar procedure as the one detailed in [16], Fox-H [32] function is identified after employing the Mellin transform along with some of its properties. In a more straightforward way, we can invoke [Eq.(07.34.21.0012.01), 31] if, previously, we write not only the modified Bessel function included in (16), $K_{a-b}(\cdot)$ as a Meijer-G function, as shown in Eq. (20); but also the hyperexponential function from Eq. (26) in the way indicated by [Eq. (07.34.03.0228.01), 31].

$$G_{0,1}^{1,0}\left(b\gamma_0^c I^{2c}\middle|\begin{matrix}-\\ 0\end{matrix}\right)=\exp\left[-b(\gamma_0 I^2)^c\right]. \tag{28}$$

Now it is possible to use [Eq. (07.34.21.0012.01), 31] to solve Eq. (27) as

$$P_b(e) = \frac{a}{[\det(\mathbf{A})]^{\alpha}\Gamma(\alpha_x)} \sum_{i=1}^{N'} \sum_{m=1}^{\alpha_i} \frac{1}{\Gamma(m)} \frac{\lambda_i^{\frac{m-\alpha_x}{2}} \alpha_x^{\frac{m+\alpha_x}{2}}}{(\alpha_i - m)!} \times \sum_{k_1+\ldots\overset{i}{\ldots}+k_{N'}=\alpha_i-m} \binom{\alpha_i - m}{k_1 \ldots \overset{i}{\ldots} k_{N'}} \prod_{\substack{j=1 \\ j\neq i}}^{N'} \left[(-1)^{k_j} (\alpha_j)_{k_j} \left(\frac{-1}{\lambda_i} + \frac{1}{\lambda_j} \right)^{-\alpha_j - k_j} \right] \times \left(\frac{\alpha_x}{\lambda_i} \right)^{-\left(N\alpha - \frac{m-\alpha_x}{2} + \sum_{\substack{j=1 \\ j\neq i}}^{N'} [-\alpha_j - k_j]\right)} H_{2,1}^{1,2} \left(\frac{b\gamma_0^c \lambda_i^{2c}}{\alpha_x^{2c}} \middle| \begin{matrix} \hat{A}, \hat{B} \\ (0,1) \end{matrix} \right), \tag{29}$$

where

$$\hat{A} = (1 + \sum_{\substack{j=1 \\ j\neq i}}^{N'} [\alpha_j + k_j] - N\alpha, 2c),$$
$$\hat{B} = (1 + \sum_{\substack{j=1 \\ j\neq i}}^{N'} [\alpha_j + k_j] - N\alpha + m - \alpha_x, 2c).$$

In Eq. (29), $H_{ij}^{kl}(\cdot)$ represents the Fox-H function, a generalization of the Meijer-G function introduced in [33] and defined from the Mellin-Barnes integral. We must remark that the expression obtained in (29) is completely generic, valid for any turbulent regime, any degree of correlation among channels, any number of receivers and geometric topology and whatever coding and modulation technique will be used,as long as it can be adjusted with this numerical method.

5. RESULTS AND DISCUSSION

In this section, we present some Monte-Carlo numerical results for different turbulence conditions used to corroborate the validity of the ABER expressions proposed in this paper. It is worth mentioning that we have used the code given in [Appendix E, 34] to numerically evaluate the special functions (Meijer-G and Fox-H functions) included in the equations derived in this work. In addition, we must recall we have always considered point detectors in this paper for which turbulence-induced signal fluctuations can be quite deleterious to system performance. Accordingly, we implement a method based on the Cholesky decomposition on the covariance matrix $\mathbf{C_y}$, for generating correlated gamma random variables. That method is performed by matching their first and second moments, as detailed in [35]. Finally, we must mention the way we use Eq. (7). Thus, following Fig. 3, we obtain the definition of the correlation factor from Eq. (7) by taking into account that small-scale contributions to scintillation are associated with turbulent cells smaller than the first Fresnel zone or the transverse spatial coherence radius, ρ_0 given in Eq. (6), whichever is smallest [30]. Hence the smallest value from both magnitudes will determine the definition of Eq. (7) employed in the results presented in this paper. As detailed in previous sections, we supposed that large-scale fluctuations are common for all the receivers, an approximation completely consistent with the receiving areas considered in this paper (30 and 60 cm^2) where the point photodetectors will be distributed, as it details below. Lastly, the figures of results shown in this Section and involving BER performance will represent the OOK transmission scheme unless noted otherwise. In all those figures, the numerical results are represented by circles to demonstrate the validity of the analytical expressions developed in the previous section.

Figure 4 shows the analytical results corresponding to the two extreme cases represented in Eqs. (23) and (24). The forward error correction (FEC) technique limit is displayed as a reference, indicating an ABER$\leq 3.8 \times 10^{-3}$. That FEC (with only 7 % of overhead) with an ABER limit of ABER$\leq 3.8 \times 10^{-3}$ for hard decision [36] is widely adopted in many communication systems including those operating at optical frequencies on atmospheric [37–41] or even underwater turbulence [42]. This ABER limit represents the error-free transmission regime when FEC is employed.. Moreover, for terrestrial systems the International Telecommunication Union (ITU) has also standardized a 7% coding overhead (to guarantee interoperability of systems) [43]. In this case, the standard FEC scheme uses the ITU standard Reed Solomon code RS(255,239). Other options are, for example, to employ enhanced FEC where several codes are serially concatenated with a certain interleaving depth and some iterations of decoding are used to improve the error correction capability, what adds a 7% data rate overhead and provides more than 8 dB of gain [38].

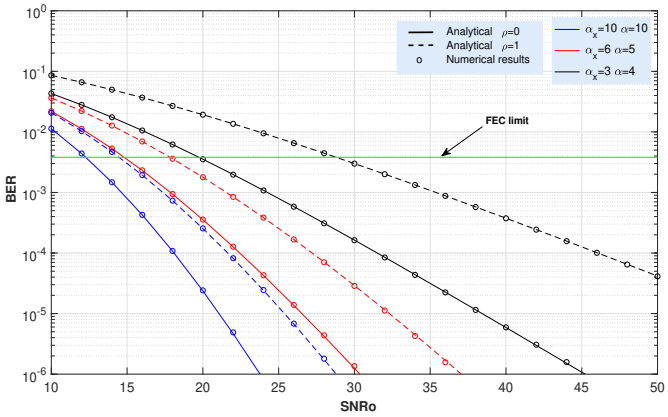

Fig. 4. BER vs. average electrical SNR for extreme small-scale correlation cases $p = 0$ y $p = 1$. $N = 3$ receivers for $C_n^2 = 4 \times 10^{-15}$, $C_n^2 = 10^{-14}$ y $C_n^2 = 10^{-13}$ m$^{-2/3}$, related to conditions of weak, moderate and strong turbulence, respectively.

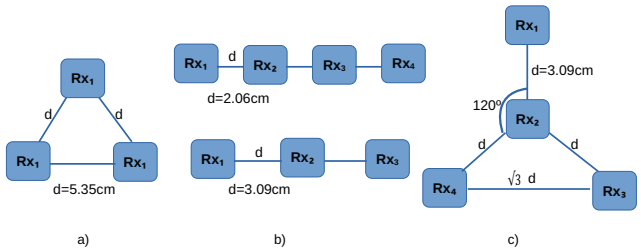

Fig. 5. Configuration of receivers and obtained separation among them considering a fixed circle area of 30 cm^2 in reception for three different correlation models called constant (a), exponential (b) and star (c) models.

Coming back to that aforementioned ABER limit of 3.8×10^{-3}, for such a reference, a difference of 2.2 dB and 9 dB in SNR$_0$ is obtained when considering weak and strong turbulence, respectively. As expected, a better performance is obtained when employing non-correlated small-scale scintillations and weak atmospheric turbulence.

However, in many situations it is not realistic to consider totally uncorrelated channels. On the contrary, the separation between receivers determines the degree of correlation associated to the sequences of power received by them. Therefore, the adoption of a particular physical configuration (topology)

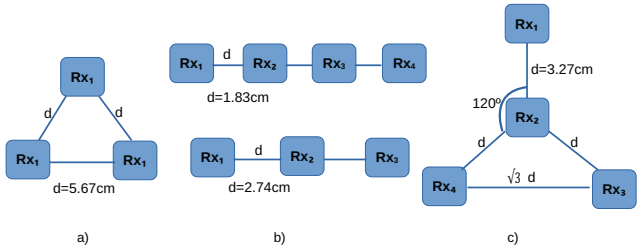

Fig. 6. Configuration of receivers and obtained separation among them considering a fixed square area of 30 cm^2 in reception for three different correlation models called constant (a), exponential (b) and star (c) models.

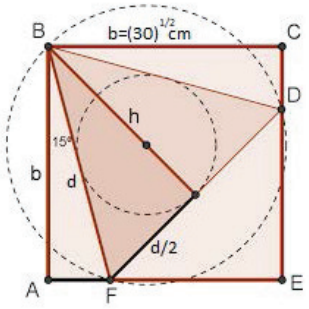

Fig. 7. The constant correlation model inside a square area of 30 cm^2. Photodetectors are placed on nodes 'B', 'D' and 'F'.

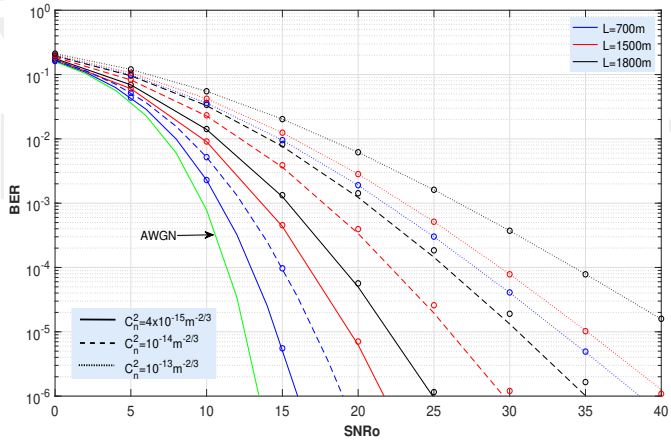

Fig. 8. BER vs. average electrical SNR for the constant model of correlation with receiving square area of 30 cm^2 and $N = 3$ receivers. Results are shown for weak, moderate and strong turbulence, $C_n^2 = 4 \times 10^{-15}$, $C_n^2 = 10^{-14}$ and $C_n^2 = 10^{-13}$ m$^{-2/3}$, respectively, and link lengths of 700 m, 1500 m and 1800 m.

of photoreceivers may impact on the overall performance of the link, In this paper, we have analyzed the three different topologies depicted in Fig. 2 with the purpose of both offering a realistic scenario and weighting the impact of the separation distance among receivers. Moreover, the receivers are included in a same fixed area of 30 cm^2, with two different shapes: a circle surface and a square one. Thus Figures 5 and 6 show the obtained maximum separation distances for both scenarios. For instance, Figure 7 shows how to obtain the maximum separation distance among photodetectors in a square surface of 30 cm^2.

In this respect, Figure 8 shows the analytical simulation for the BER associated with the constant correlation model, as indicated in Eq. (3), with the receivers distributed in a fixed square

Link Lengths	700m	1500m	1800m
	$p \mid \rho_I$	$p \mid \rho_I$	$p \mid \rho_I$
$C_n^2 = 4 \times 10^{-15}$	0.052|0.507	0.251|0.610	0.316|0.644
$C_n^2 = 10^{-14}$	0.052|0.491	0.251|0.598	0.316|0.633
$C_n^2 = 10^{-13}$	$\longrightarrow$ 0|0.375	$\longrightarrow$ 0|0.375	$\longrightarrow$ 0|0.375

Table 2. Small-scale correlation factors, p, and total correlation factor, ρ_I, using the constant correlation model with 30 cm^2 of square area, for the proposed link lengths considering weak, moderate and strong turbulence, $C_n^2 = 4 \times 10^{-15}$, $C_n^2 = 10^{-14}$ and $C_n^2 = 10^{-13}$ m$^{-2/3}$, respectively.

Link Length	700m	1500m	1800m
	$p \mid \rho_I$	$p \mid \rho_I$	$p \mid \rho_I$
$C_n^2 = 4 \times 10^{-15}$	0.072|0.517	0.292|0.632	0.359|0.666
$C_n^2 = 10^{-14}$	0.072|0.502	0.292|0.620	0.359|0.656
$C_n^2 = 10^{-13}$	$\longrightarrow$ 0|0.375	$\longrightarrow$ 0|0.375	$\longrightarrow$ 0|0.375

Table 3. Small-scale correlation factors, p, and total correlation factor, ρ_I, using the constant correlation model with 30 cm^2 of circle area, for the proposed link lengths considering weak, moderate and strong turbulence, $C_n^2 = 4 \times 10^{-15}$, $C_n^2 = 10^{-14}$ and $C_n^2 = 10^{-13}$ m$^{-2/3}$, respectively.

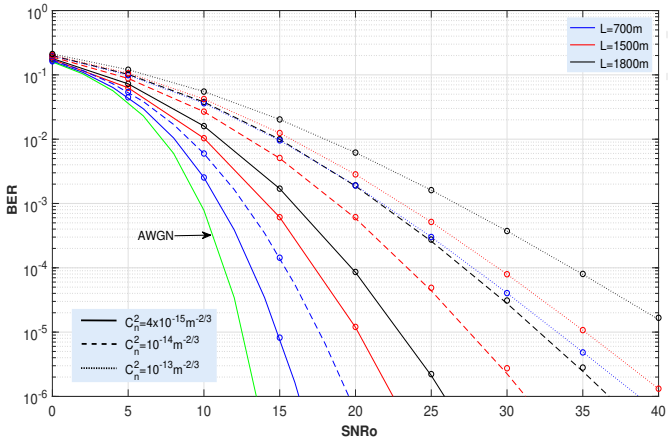

Fig. 9. BER vs. average electrical SNR for the exponential model of correlation with square area of 30 cm^2 and $N = 3$ receivers. Results are shown for weak, moderate and strong turbulence, $C_n^2 = 4 \times 10^{-15}$, $C_n^2 = 10^{-14}$ and $C_n^2 = 10^{-13}$ m$^{-2/3}$, respectively, and link lengths of 700 m, 1500 m and 1800 m.

area, whereas the values obtained from the small-scale correlation, p, and total correlation, ρ_I, are shown in Table 2 according to Eqs. (11) and (15). In addition, as in the rest of the simulations, conditions of weak, moderate and strong turbulence have been considered, with $C_n^2 = 4 \times 10^{-15}$ m$^{-2/3}$, $C_n^2 = 10^{-14}$ m$^{-2/3}$ y $C_n^2 = 10^{-13}$ m$^{-2/3}$, respectively, as well as three different path lengths of $L = 700$ m, $L = 1500$ m y $L = 1800$ m. For the sake of clarity, the performance of an ideal AWGN channel is added as a reference. We can observe how the longer the propagation path length, the worse the performance we obtain. For example, for a

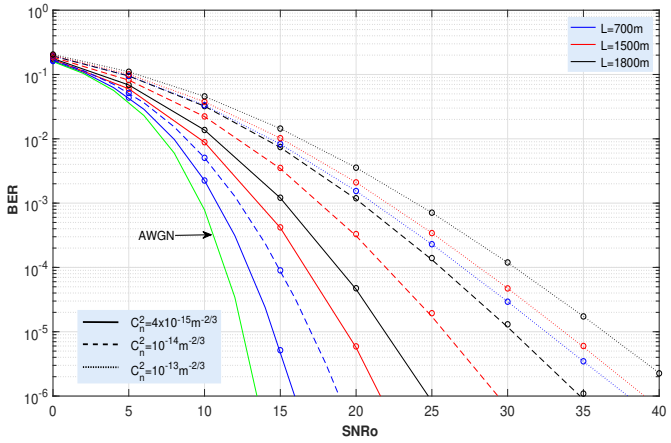

Fig. 10. BER vs. average electrical SNR for the star model of correlation with square area of 30 cm^2 and $N = 4$ receivers. Results are shown for conditions of weak, moderate and strong turbulence, $C_n^2 = 4 \times 10^{-15}$, $C_n^2 = 10^{-14}$ and $C_n^2 = 10^{-13}$ m$^{-2/3}$, respectively, and link lengths of 700 m, 1500 m and 1800 m.

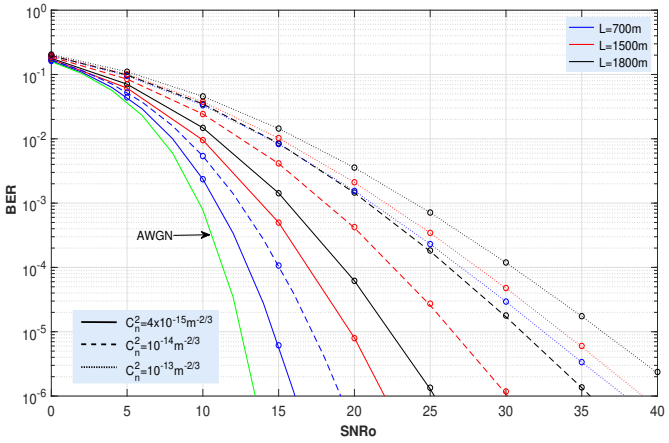

Fig. 11. BER vs. average electrical SNR for the star model of correlation with circle area of 30 cm^2 and $N = 4$ receivers. Results are shown for conditions of weak, moderate and strong turbulence, $C_n^2 = 4 \times 10^{-15}$, $C_n^2 = 10^{-14}$ and $C_n^2 = 10^{-13}$m$^{-2/3}$, respectively, and link lengths of 700 m, 1500 m and 1800 m.

strong turbulence regime, and considering a separation between receivers of $d = 5.35$ cm (Fig. 5a), the results get worse as the length of the link increases. Such performance can be improved when the different channels are becoming more uncorrelated.

Since the difference in separation distance between correlative photodetectors when using a circle surface is barely 0.32 cm in respect of the case of employing a square area (both fixed to 30 cm^2), their associated behaviors are not showing a significant difference and, therefore, Fig. 8 can represent both cases. Accordingly, and related to that small difference in separation distance between receivers, the correlation coefficients present similar values for a circle area (see Table 3) than those for a square surface.

On the other hand, Figure 9 depicts the obtained behavior for the exponential correlation model and a square area of 30 cm^2. If such the Fig. 9 is now compared to Fig. 8, we can appreciate a slight improvement of this latter topology in respect of the exponential one, from 0.75 dB for the case of $C_n^2 = 4 \times 10^{-15}$ m$^{-2/3}$ and $L = 700$ m for an error probability of 10^{-5}; to around 3 dBs for $C_n^2 = 10^{-14}$ m$^{-2/3}$ and $L = 1800$ m for that same value of error probability. The curves representing $C_n^2 = 10^{-13}$ m$^{-2/3}$ remain the same since the correlation factor affecting them in both topologies is tending to 0 for the small scale fluctuation (totally uncorrelated small scale scintillations). As in the constant correlation model, the use of either a circle surface or a square one hardly induces a slight change in performance (better when a circle area is employed since the distance between correlative receivers is larger).

Lastly, the results obtained from the star receiver topology are shown in Fig. 10, with $N = 4$ receivers spread in a square area of 30 cm^2. For this case, we also offer the results of the same scenario but distributing the photodetectors in a circle area (Fig. 11), instead of a square one. A slight improvement in performance is observed again when considering a square surface (corresponding to the increase of barely 0.18 cm in d, see Figures 5 and 6); except for the case of $C_n^2 = 10^{-13}$ m$^{-2/3}$ since, as we explained above, the channels are totally uncorrelated for that value of the structure parameter.

In order to better understand the behavior of these systems, Figure 12, shows the comparison in performance when employing $N = 3$ receivers with regard to $N = 4$, when those receivers have been distributed in a circle area and following an exponential correlation model. Here we can appreciate an important feature. Figures 12a and 12b are not showing difference in performance when increasing the number of photodetectors from $N = 3$ to $N = 4$, except for the case of considering all the small-scale effects totally uncorrelated (dotted lines). This fact means that it is not justified to enlarge the complexity of the system when the available space is reduced (30 cm^2 in the scenario taken as illustrative example). As seen in Fig. 5, the separation distance between receivers is reduced from 3.09 cm ($N = 3$) to 2.06 cm ($N = 4$). The reduction in separation distance implies an increase in the magnitude of the correlation factor between photodetectors that compensates the benefit of increasing the number of photoreceivers. Nevertheless, when this limitation is overcome and it is feasible to add a new photodetector while maintaining the separation distance between correlative receivers, then an improvement in performance is appreciated as shown in Fig. 12c, more remarkable when longer such separation distance.

On the other hand, the ABER of vw-MPPM coding transmission is discussed from the results obtained from Eq. (29), numerically validated via Monte-Carlo simulation. Thus, Fig. 13b shows the results obtained when using Eq. (29) with a 2/3 code rate. They are compared to the ones depicted in Fig. 13a and extracted from Eq. (22) for a classic OOK modulation. A constant correlation model considering a circle area of 30 cm^2 was employed, where the photodetectors are separated $d = 5.35$ cm according to Fig. 5a. Succinctly, an improvement of around 7 dB in average can be measured between the performance associated to the vw-MPPM case (Fig. 13b) compared to the OOK one (Fig. 13a) for an ABER of 10^{-5}. Evidently, the improvement in performance associated to the vw-MPPM technique is at the expense of a reduction in the data rate by a factor 1/3. Lastly, the numerical simulation corroborates the validity of Eq. (29) for any condition (correlation factor, topology, turbulence regime, ...) and coding and modulation techniques.

A similar comparison was performed in Fig. 14, including

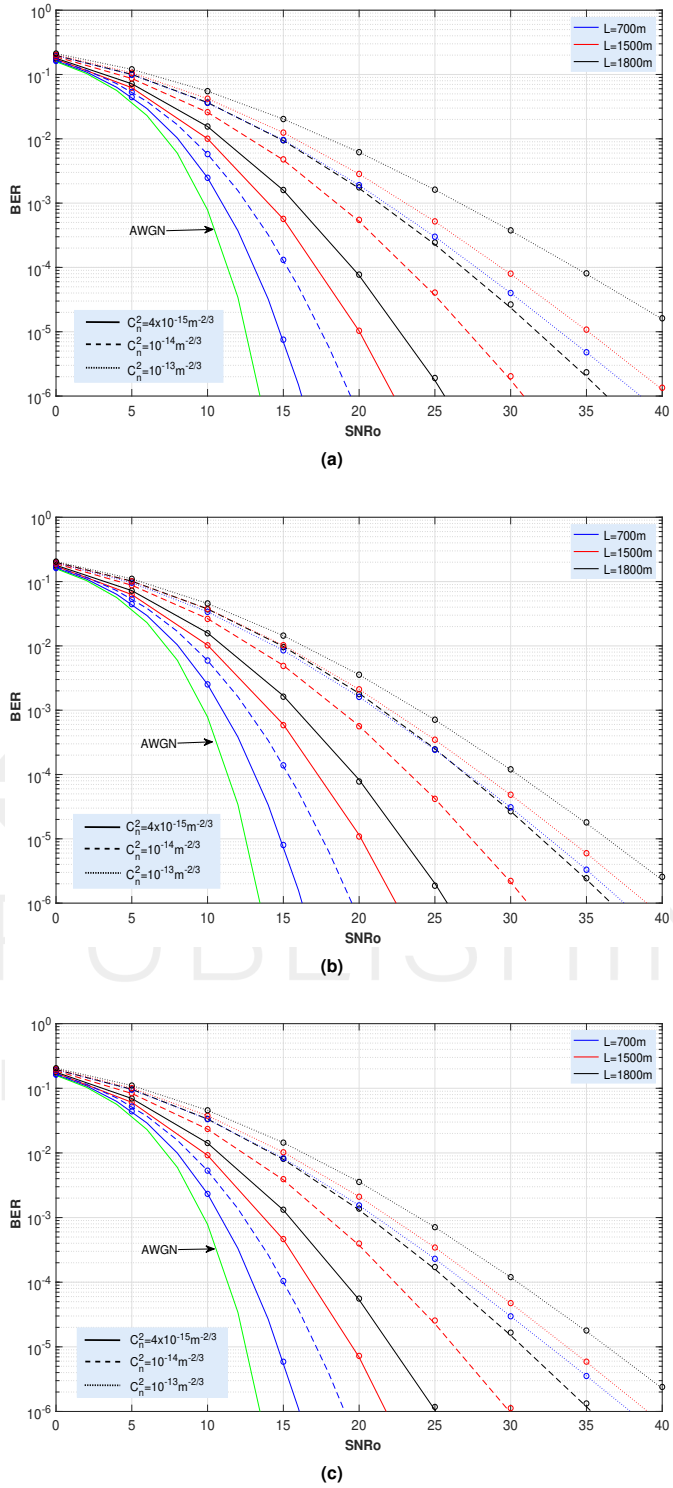

Fig. 12. Comparation of BER vs. average electrical SNR for the exponential model of correlation with receiving circle area of 30 cm^2, using $N = 3$ receivers, (a), and $N = 4$ receivers, (b). In addition, the case of $N = 4$ receivers with each pair of consecutive receivers separated 3.09 cm is shown in (c)

an exponential correlation model with a 60 cm^2 circle area, with $N = 2$ and $N = 4$ receivers, and assuming a strong turbulence regime. An improvement of around 6 dB in average was registered in favor of the vw-MPPM scheme in relation to the OOK modulation at the reference BER of 3.8×10^{-3}.

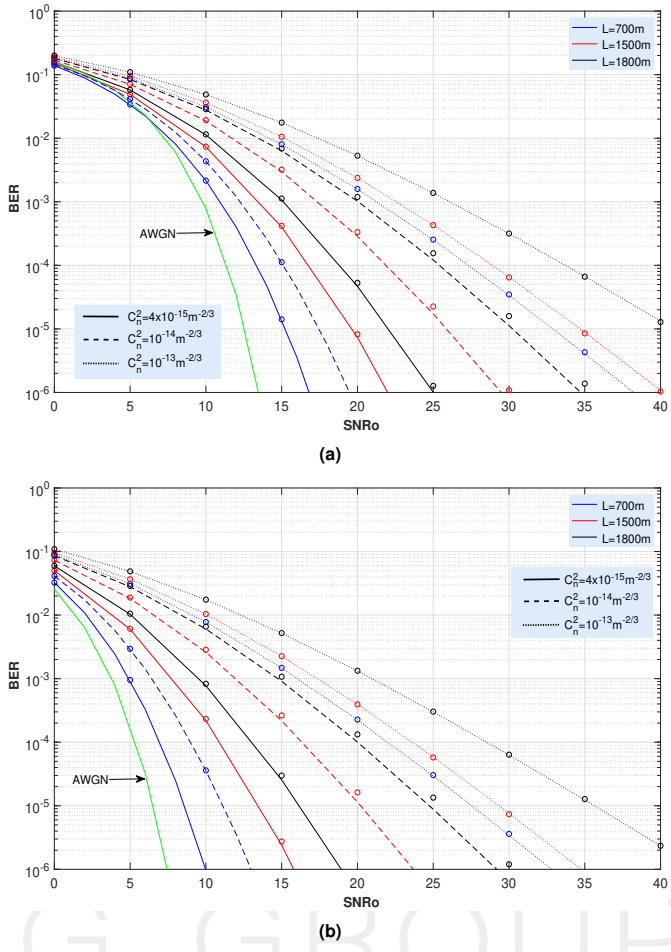

Fig. 13. BER vs. average electrical SNR for the constant model of correlation with a 30 cm^2 circle area and $N = 3$ receivers, using OOK (a), and vw-MPPM with 2/3 code rate, (b).

As a remarkable comment, the areas considered in this work are aligned to current commercial solutions: for instance, a 30 cm^2 aperture is similar to the one implemented by SONAbeam® Z series (50 mm diameter); whereas a 60 cm^2 area is a magnitude close to SONAbeam® E series (10 cm diameter) [44].

Finally, we want to recall that our paper is intended to consider point receivers, where turbulence-induced signal fluctuations are affecting the system performance with its maximum adverse effect. Certainly, this would be true if the receiving aperture in an optical communication system is smaller than the correlation width of the irradiance fluctuations, ρ_c. If a receiving aperture of diameter D is larger than that latter scale size, the receiver will average the fluctuations over the aperture and the scintillation will be less compared to scintillation measured with a point receiver [45]. Aperture sizes larger than ρ_c will experience some form of "aperture averaging," which in effect reduces the scintillation experienced by the receiver photodetector. Hence, and from Eq. (7), it is possible to distinguish two different situations: first, for the case of weak conditions, the correlation scale of the irradiance fluctuations is defined by the size of the Fresnel zone ($\sqrt{\lambda L}$ in this paper); thus, significant aperture averaging takes place only when $D > 2\sqrt{\lambda L}$. Second, for strong turbulence conditions, that correlation scale

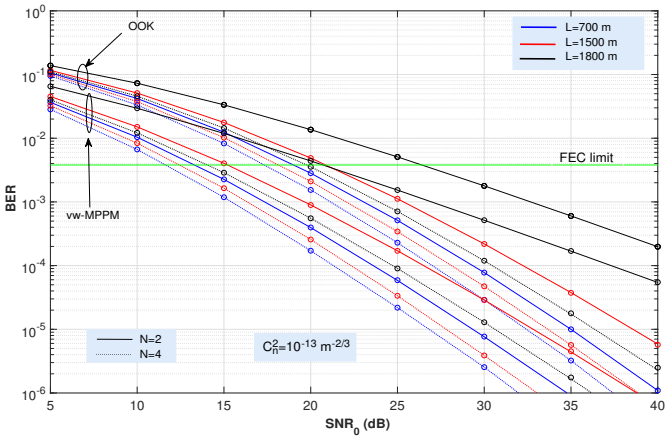

Fig. 14. BER vs. average electrical SNR for the exponential correlation model with receiving circle area of 60 cm^2, for $N = 2$ and 4 receivers. Results are shown for $C_n^2 = 10^{-13}$ m$^{-2/3}$ (strong turbulence), and link lengths of 700 m, 1500 m and 1800 m.

is determined first by the spatial coherence scale ρ_0, as we have discussed in Section 2.C. Same conclusions are derived in [46]. In this respect, and for the magnitudes considered in our paper, the detectors could be considered as point detectors if 1) for the case of weak turbulence regime, the separation between two correlative receivers is $D < 2\sqrt{\lambda L}$ i.e., $D < 6.5$ cm ($L = 700$ m), 9.6 cm ($L = 1500$ m) and 10.56 cm ($L = 1800$ m); and 2) for the case of for strong turbulence regime, the separation between two correlative receivers must be $D < \rho_0$ i.e., $D < 2.32$ cm (L=700 m), 1.48 cm ($L = 1500$ m) and 1.32 cm ($L = 1800$ m).

Thus, from the configuration of receivers employed in our paper (Figs. 5 and 6), the maximum distance between receivers is 5.67 cm (corresponding to the constant configuration with three receivers shown in Fig. 6(a) in our paper). For that scale size, we are in the limit of considering point receivers for all the cases of weak ($C_n^2 = 4 \times 10^{-15}$ m$^{-2/3}$) and moderate ($C_n^2 = 10^{-14}$ m$^{-2/3}$) turbulence, and including the three different propagation path lengths considered in the paper for these two values of structure parameters in addition to any of the spatial configuration of receivers analyzed in our paper for a receiving area of 30 cm^2.

However, for the case of strong turbulence ($C_n^2 = 10^{-13}$ m$^{-2/3}$), the supposition of point detectors does not hold. In this case, the assumption of having point receivers is only intended for showing the maximum adverse effects from the turbulent atmosphere. This assumption is also taken into account in many other papers [21, 24], especially when studying systems based on an intensity modulation and direct detection (IM/DD) scheme (as in this paper) for which the irradiance fluctuations are primarily concerned.

6. CONCLUSIONS

In this work, a complete analysis of the performance associated to a SIMO configuration with spatial diversity has been performed in realistic scenarios. The derived analytical expressions for the ABER are obtained in terms of the correlation length of the received irradiance fluctuations, and depending on the propagation path length, the refractive index structure parameter or the impact of the correlation matrix of the small scale scintillations on the overall performance, assuming that the large-scale turbulence-induced fading is a common contribution for all of the receivers. Precisely such the correlation matrix is also depending on the separation distance between photodetectors, i.e., the correlation factors are not fixed to certain values for academic purposes, but calculated in a realistic way from the configuration of the FSO link, the number of photodetectors or the physical available space in reception. Moreover, the correlation length, in addition, is determined by comparing the magnitudes of the spatial correlation value and the first Fresnel zone, according to Fig. 3.

Furthermore, three illustrative spatial geometries of receivers were considered [17, 19], giving rise to three small-scale correlation matrices which characterize the correlation between the fading signals in each of the diversity branches: constant, exponential and star correlation models. Indeed, a topology will present better performance if the separation distance among its photodetectors is larger, as corroborated in this paper. For instance, the configuration with a constant correlation model presents better performance than the obtained from an exponential correlation model with $N = 3$ photodetectors since their separation distances are shorter than the ones achieved for the constant model, assuming a same fixed surface (identical magnitude and identical geometric shape) to distribute the photodetectors. Same conclusions can be obtained when comparing the star topology in relation to the exponential one. Since the received area considered in this work is not very large (typically 30 cm^2, or even 60 cm^2), difference in behavior among topologies are not remarkable (around 2−3 dBs for an ABER of 10^{-5}). It is expected to obtain a more remarkable difference when that area becomes larger.

On another note, and regarding the limited physical available space in the receiver side for distributing the photodetectors, there may exist situations as the one shown in Figs. 12a and 12b where the whole FSO system is not experimenting any improvement in performance when adding new photodetectors. The underlying reason resides in the short separation distance among photodetectors and, consequently, the correlation factor becomes larger, countering the benefit of having more different diversity branches in the considered EGC spatial diversity technique. Of course, if totally uncorrelated channels are supposed, then the addition of new photoreceivers always improves the performance of the system.

Finally, we have incorporated the study of the vw-MPPM as an illustrative example of a generic nonlinear block coding technique whose CBER cannot be derived in a closed-form expression. Its analysis was carried out by employing a hyperexponential fitting procedure. Here, the improvement in performance with respect to OOK scheme is more remarkable as vw-MPPM includes a rate-adaptive transmission scheme using block coding and thus, increasing its resulting PAOPR. These results, and the rest of them included in this paper, corroborate the validity of the derived analytical expressions.

APPENDIX A

In this Appendix, the assumption of common large-scale effects affecting all the receivers is discussed in detail. From the early works published by Taylor [47], based on some measurements of intensity and scale inside wind-tunnels [48]; or by Kolmogorov [49], with a turbulent flow composed by “eddies” of different sizes, we know some features that can justify this approach. Thus, for example, near the ground, the value of the outer scale of turbulence is thought to be comparable with the height above ground (around 20 or 30 m if we consider a typical scenario with

the transceivers over two different buildings), much larger than either the beam waist propagating through the atmosphere or the radius of the receiver. In this respect it seems that when the turbulent process begins, the approach of considering a common large-scale effect for all the receivers becomes real.

Then, the energy is input at small wave numbers and dissipated at much larger wave numbers. In this wave number range called the inertial subrange, the Reynolds number is so high for the large eddies that they are unstable and break apart. Thus they transfer energy to smaller scales (higher wave numbers) down to the inner scale of turbulence l_0, a scale of only a few millimeters where the Reynolds number approaches unity and the energy is dissipated into heat. This heat is seen as the starting point to begin a new turbulent process. All these features in combination with Taylor's hypothesis (eddies staying in the same place for a long time compared to the typical data rates, and moving as a whole) allows us to think of having a varying number of large-scale eddies in the link affecting all the receivers at the same time, as we will show below.

In addition, Tatarskii [22, 50] predicted that the correlation length of the irradiance fluctuations is on the order of the first Fresnel zone. On the other hand, measurements [51, 52] of the irradiance covariance function under strong-fluctuation conditions revealed that the correlation length decreases when increasing the Rytov variance and that a large residual correlation tail emerges at large separation distances. Id est, in the strong-fluctuation regime the correlation length of irradiance fluctuations is determined by the spatial coherence radius ρ_0 (see Eq. (6)) of the optical wave, whereas the width of the residual tail is characterized by the scattering disk calculated as $L/(k\rho_0)$, with L denoting the propagation path length and with k being the wave number of optical radiation. All these parameters (size of the Fresnel zone, the spatial coherence radius and the scattering disk and a comparative with the received beam waist) will be discussed more in detail later.

Furthermore, the sets of observations made about irradiance measurements in [53, 54] contributed to understand and develop expressions for the large-scale and small-scale irradiance covariance functions. The two-scale process associated with scintillation is described in detail in [55] and discussed in [56]. Moreover, all these findings help Andrews et al.[20] to develop an heuristic model of irradiance fluctuations for a propagating optical wave in a weakly inhomogeneous medium under the assumption that small-scale irradiance fluctuations are modulated by large-scale irradiance fluctuations of the wave. There, the upper bound for small turbulent cells was defined by the smallest cell size between the Fresnel zone and the transverse spatial coherence radius, ρ_0, of the optical wave; whereas the lower bound for large turbulent cells was defined by the largest cell size between the Fresnel zone and the scattering disk.

To conclude this review of theory of optical scintillation based on experimental observations, we recently proposed and developed in [57] a new statistical model for the turbulence, the Málaga model (seen as a generalization of the gamma-gamma one) whose physical model was presented in [58] after a deeper interpretation of such the Málaga model. In this respect, its propagation model and the turbulence induced scintillation effects can be physically interpreted as the superposition of several generalized-K sub-channels corresponding each one to a different physical optical path. It was demonstrated (and validated with Monte-Carlo simulations) that the large-scale fading characteristic associated to each sub-channel is established by α_x defined in Section 2 (the same parameter than in a gamma-gamma model, and related to the effective number of large-scale cells of the scattering process, as discussed in [27]) and, as expected, it is common for every generalized-K terms. In contrast, the small-scale fluctuations depend on the specific subchannel, where the more severe conditions, the lower the probability of the optical power to be coupled to the line-of-sight (LOS) component. Even more, different optical sub-channels may be associated to a different turbulence condition. An additional feature comes from the probability that certain portion of the optical signal travels through the $k-$th optical path. This probability was demonstrated to follow a Binomial distribution [58] depending on the parameters of that Málaga distribution (many of them coincident to their corresponding ones in the gamma-gamma distribution) that configure the probability for the optical power to be coupled to the LOS component. It means that large-scale fluctuations associated to large-scale cells of the scattering process will have a higher or a lower weight in the final received fluctuating intensity depending on either the probability for the optical signal traveling through a concrete subchannel as well as on the optical power distribution among the contributing sub-channels.

All the arguments related above support our initial assumption, and now it is possible to evaluate its accuracy. The idea is not new since in [Figure 6, 59] it is shown the propagation geometry of an optical wave through the turbulent atmosphere, where common eddies inducing correlated deflection into all the receivers were included. In that paper, the authors give a physical recalling that channel correlation arises mainly from the deflection effects of the large-scale eddies whose sizes are larger than the scattering disk, consistent with what we have detailed above. Those common eddies simultaneously deflect the light in both the two channels considered in [59] and thus generate the channel correlation; in contrast, the independent eddies only modify the light in one channel and thus degrade the correlation. With increasing turbulence strength, the spatial coherent radius decreases [30] and hence the scattering disk increases. Therefore the average size of the large-scale eddies is increased. Accordingly, the probability of interacting with common eddies increases, although for this case, we must compare that average size of the large-scale eddies with the beam waist of the optical transmitted signal, wider as a consequence of the stronger turbulence regime.

A similar model is applied in [60]. There, it is concluded that if either the propagation path length is much larger than the laser beam divergence, and if the receivers are sufficiently close, then the signals received by the photodetectors are likely to be deflected by the same eddies, implying that large-scale effects can be assumed to be the same for all the receivers. In addition, the width of the light beam issued by a transmitter laser expands as the propagation path length increases. This effect is depicted in [Fig. 2(a), 61] that we include here in Fig. 15 for the sake of completeness.

If now a horizontal FSO transmission with a Gaussian profile for the beam intensity is considered [62], the radius of that beam, at a distance z from the laser source, is given by [30]

$$W_e(z) = W(z)\sqrt{1 + 1.625\sigma_R^{12/5}\Lambda}, \tag{30}$$

where $\sigma_R^2 = 1.23C_n^2k^{7/6}L^{11/6}$ is the Rytov variance, with C_n^2 being the refraction index structure parameter, which is directly related to the turbulence strength, with k being the wave number and with L representing the propagation path length. Moreover, $\Lambda = 2z/(kW^2)$ with z being the propagation distance, with W being the beam radius at $z = L$, whereas the generic expres-

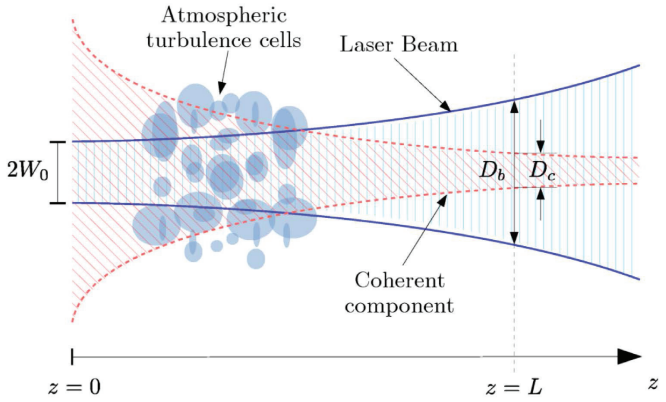

Fig. 15. Propagation model of a partially coherent Gaussian laser beam: W_0 is the initial beam radius, $D_b = 2W_e$ is the beam diameter and $D_c = 2\rho_0$ is the transverse coherence diameter, both at $z = L$. Figure taken from [61].

sion for $W(z)$, the beam radius in the absence of turbulence, is defined by

$$W(z) = W_0\sqrt{\left(1 - \frac{z}{F_0}\right)^2 + \left(\frac{2z}{kW_0^2}\right)^2}. \quad (31)$$

In Eq. (31), W_0 is the beam radius at the $1/e$ point of the field ($1/e^2$ of the irradiance) at the transmitter, F_0 is the phase front radius of curvature at the transmitter output (we can consider a collimated beam, i.e. $F_0 \to \infty$), $k = 2\pi/\lambda$ is the wave number and λ is the wavelength. In this paper, we have considered $\lambda = 1550$ nm, three different magnitudes for the structure parameter: $C_n^2 = 4 \times 10^{-15}$, 10^{-14} and 10^{-13} $m^{-2/3}$; and three different propagation lengths: $L = 700$, 1500 and 1800 m. Moreover, we can assume $W_0 = 2.5$ cm, as in [30]. Then, operating, we obtain the representative values included in Table 4.

From Table 4, the beam waist at the receiver will vary from 2.5 cm ($W_e = W_0$ since the optical beam is affected by a very weak turbulence regime) to 31.7 cm (strong turbulence and the longest path, $L = 1800$). From Eq. (7), the correlation lengths (which describes the average speckle size at the receiver) are taking the values of 3.3, 4.8 and 5.3 cm (when approaching its value to $\sqrt{\lambda L}$) for weak turbulence and $L = 700$, 1500 and 1800 m, respectively; while, for strong turbulence and same values of L, respectively, their values are 1.16, 0.74 and 0.66 cm. From Figure 3, we can see how the cases of $C_n^2 = 4 \times 10^{-15}$, and $C_n^2 = 10^{-14}$ $m^{-2/3}$, for all the propagation path lengths considered (700 m, 1500 m and 1800 m) can be considered as weak fluctuations since the value of the Fresnel zone is below the curves representing the coherence radius for $C_n^2 = 4 \times 10^{-15}$ and $C_n^2 = 10^{-14}$ $m^{-2/3}$. Additionally, it is reasonable to think that since the average speckle size at the receiver is larger than the received beam waist, and, moreover, from Figures 5 and 6, the radius of the receiver is, approximately, 3 cm for each topology when considering a 30 cm^2 receiving area, then most of the large-scale fluctuations must be common for all the receivers. However, the probability that signals received in each photodetector pass through the same eddies (common eddies) decreases for strong turbulence since the channel correlation decreases as both L and C_n^2 increase. In this case, the average speckle size (i.e., the correlation length) is smaller than the beam waist and small-scale fluctuations (diffractive effects) are most noticeable. In this respect, our assumption (common large-scale fluctuations for all the receivers) turns into a worst case of performance, showing an upper error bound obtained for a particular FSO link under design.

Following [30], large-scale fluctuations in the irradiance are generated by turbulent cells larger than that of the first Fresnel zone or the scattering disk $L/(k\rho_0)$, whichever is largest. From the values included in Table 4, we can see how the sizes of cells inducing large-scale fluctuations are larger than 3.3 cm ($L = 700$ m), 4.8 cm ($L = 1500$ m) and 5.3 cm ($L = 1800$ m) for $C_n^2 = 4 \times 10^{-15}$ $m^{-2/3}$ and $C_n^2 = 10^{-14}$ $m^{-2/3}$; whilst for the case of $C_n^2 = 10^{-13}$ $m^{-2/3}$, large-scale fluctuations are caused by cells with sizes larger than 3.3 cm (still $\sqrt{\lambda L}$ dominating for $L = 700$ m), 5.03 cm ($L = 1500$ m) and 6.74 cm ($L = 1800$ m), these two latter path lengths dominated by the scattering disk. Again, we recall we have adopted in this paper a more restrictive value for the Fresnel zone size, $\sqrt{\lambda L}$. It means that, if we compare these eddy sizes (for $C_n^2 = 4 \times 10^{-15}$ $m^{-2/3}$ and $C_n^2 = 10^{-14}$ $m^{-2/3}$) to those scale sizes characterizing $W_e(L)$ for the same two structure parameter values, and considering that the correlation length also indicates the average size of the turbulent cells, then we can extract the following conclusions:

1. Following [56], if $\rho_0 > \sqrt{L/k}$, then the coherence length is greater than the first Fresnel zone, and the magnitude $\sqrt{\lambda L}$ is the size of the dominant inhomogeneities producing scintillations. Cell sizes involved in large-scale fluctuations of intensity for $C_n^2 = 4 \times 10^{-15}$ $m^{-2/3}$ and $C_n^2 = 10^{-14}$ $m^{-2/3}$ are larger than the received beam waist for all the lengths considered in this paper. Their average sizes imply that the probability of having a cell of that average size (and even larger) is high. For example, for the case of $C_n^2 = 10^{-14}$ $m^{-2/3}$ and $L = 1500$ m, the average eddy size is 4.8 cm, almost twice larger as the size of the beam waist at the receiver, i.e., $W_e = 2.78$ cm, being very likely that the transmitted optical beam can pass through turbulent cells larger than its beam waist, which is 2.78 cm at $L = 1500$ m, but less for any other position between the transmitter ($W_0 = 2.5$ cm was the supposed transmitted beam waist) and the receiver. So the approach of having a common contribution of large-scale scintillation-component for all the receivers is very accurate.

2. However, and again, from [56], if $\rho_0 < \sqrt{L/k}$, then eddies whose scale sizes are of the order of $\sqrt{\lambda L}$ are no longer causing scintillations, and the dominant scale size is ρ_0. For the case of strong turbulence considered in this paper ($C_n^2 = 10^{-13}$ $m^{-2/3}$), it is straightforward to check from Table 4 that cells contributing to large-scale scintillations are of sizes larger than 1.49 cm (L=700 m), 5.03 cm (L= 1500 m) and 6.74 cm (L=1800 m). If we compare those values with the ones for W_e (3.51 cm, 19.5 cm and 31.7 cm, respectively, for the same distances), we see how the received beam width is larger than the cell sizes from which a turbulent eddy is considered as a large-scale eddy (causing large-scale fluctuations). For this case of strong turbulence, the approach can only be seen as a mathematically tractable closed-form approximation to obtain an upper error bound in performance of any FSO system. Notwithstanding, the average dominant inhomogeneities scale size for this scenario (ρ_0, as indicated in [56] i.e., 1.16 cm, 0.74 cm and 0.66 cm for $L = 700$ m, 1500 m, and 1800 m, respectively), informs that the probability of meeting an eddy with a size larger than the ones given by the scattering disk (the minimum size to consider an

Table 4. Atmospheric link parameters.

C_n^2	L	W_e	Correlation length ($\sqrt{\lambda L}$) (average speckle size)	First Fresnel zone ($\sqrt{L/k}$)	Scattering disk ($L/(k\rho_0)$)	Spatial coherence radius (ρ_0)
4×10^{-15} m$^{-2/3}$	700 m	2.5 cm	3.3 cm (3.3 cm)	1.31 cm	0.22 cm	8.01 cm
4×10^{-15} m$^{-2/3}$	1500 m	2.53 cm	4.8 cm (4.8 cm)	1.92 cm	0.73 cm	5.07 cm
4×10^{-15} m$^{-2/3}$	1800 m	2.59 cm	5.3 cm (5.3 cm)	2.11 cm	0.98 cm	4.55 cm
10^{-14} m$^{-2/3}$	700 m	2.51 cm	3.3 cm (3.3 cm)	1.31 cm	0.37 cm	4.62 cm
10^{-14} m$^{-2/3}$	1500 m	2.78 cm	4.8 cm (4.8 cm)	1.92 cm	1.26 cm	2.93 cm
10^{-14} m$^{-2/3}$	1800 m	3.20 cm	5.3 cm (5.3 cm)	2.11 cm	1.69 cm	2.62 cm
10^{-13} m$^{-2/3}$	700 m	3.51 cm	3.3 cm (1.16 cm)	1.31 cm	1.49 cm	1.16 cm
10^{-13} m$^{-2/3}$	1500 m	19.5 cm	4.8 cm (0.74 cm)	1.92 cm	5.03 cm	0.74 cm
10^{-13} m$^{-2/3}$	1800 m	31.7 cm	5.3 cm (0.66 cm)	2.11 cm	6.74 cm	0.66 cm

eddy as a large-scale one in this scenario) is really low since the difference in size between both magnitudes is large. In this respect, the effect for this strong turbulence scenario is mostly associated to small-scale fluctuations (the Fresnel zone defines the dominant scale size for scintillation, in this case, associated to diffractive effects) and not to large-scale fluctuations. For this reason, our initial assumption (common eddies affecting all the receivers), although being here an upper bound limit, nevertheless, it should not offer a remarkable difference in respect to the real performance associated to any FSO system under study. In addition, the presence of large aerosols (rain, drizzle, fog…) in the atmosphere reduces the effective size of the largest turbulence scales, making our assumption even more realistic.

3. Saying that, from the discussion provided in [11, 20, 30], large-scale fluctuations in the irradiance are generated by turbulent cells larger than that of the first Fresnel zone or the scattering disk $L/(k\rho_0)$, whichever is largest, and can be described by the method of geometrical optics. In our case, large-scale fluctuations are caused by cells with sizes larger than 1.49 cm ($L = 700$ m), 5.03 cm ($L = 1500$ m) and 6.74 cm ($L = 1800$ m) for the case of $C_n^2 = 10^{-13}$ m$^{-2/3}$, as indicated in the previous item.

4. To support the previous item, in [63] it is also stated that the channel correlation mainly depends on the large-scale turbulence eddies rather than the small-scale turbulence eddies. For the strong turbulence regime where the scintillations are dominated by eddies whose scale sizes are given by ρ_0, shorter than the width of the first Fresnel zone, then those scintillations become independent of the turbulence intensity and the path length what, in essence, explains the saturation effect, as related in [56].

5. Finally, we have similar conditions as in [59] to ensure that channel correlation arises mainly from the deflection effects of the large-scale eddies.

ACKNOWLEDGMENT

This work was supported by the Spanish Ministerio de Ciencia, Innovación y Universidades (PID2019-107792GB-I00).

REFERENCES

1. T. R. Raddo, J. Perez-Santacruz, U. Johannsen, I. Dayoub, S. Haxha, I. T. Monroy, and A. Jurado-Navas, "FSO-CDMA systems supporting end-to-end network slicing," in *Imaging and Applied Optics Congress,* (Optical Society of America, 2020), p. JW2A.38.
2. H. Ivanov, E. Leitgeb, D. Kraus, F. Marzano, A. Jurado-Navas, S. Dorenbos, R. Perez-Jimenez, and G. Freiberger, *Free Space Optics System Reliability in the Presence of Weather-Induced Disruptions* (Springer International Publishing, Cham, 2020), pp. 327–351.
3. Z. Zhu, M. Janasik, A. Fyffe, and et al., "Compensation-free high-dimensional free-space optical communication using turbulence-resilient vector beams," Nat. Commun. **12** (2021).
4. Q. Huang, D. Liu, Y. Chen, Y. Wang, J. Tan, W. Chen, J. Liu, and N. Zhu, "Secure free-space optical communication system based on data fragmentation multipath transmission technology," Opt. Express **26**, 13536–13542 (2018).
5. G. Schimmel, T. Produit, D. Mongin, J. Kasparian, and J.-P. Wolf, "Free space laser telecommunication through fog," Optica **5**, 1338–1341 (2018).
6. S. Malik and P. K. Sahu, "Assessment of the FSO communication system using adaptive and MIMO MPPM with pointing errors and an atmospheric turbulence channel," Appl. Opt. **60**, 1719–1728 (2021).
7. L. C. Andrews, R. L. Phillips, and C. Y. Hopen, *Laser Beam Scintillation with Applications* (SPIE, 2001).
8. H. Nouri and M. Uysal, "Adaptive MIMO FSO communication systems with spatial mode switching," J. Opt. Commun. Netw. **10**, 686–694 (2018).
9. M. T. Dabiri, M. J. Saber, and S. M. S. Sadough, "On the performance of multiplexing FSO MIMO links in log-normal fading with pointing errors," J. Opt. Commun. Netw. **9**, 974–983 (2017).
10. S. M. Navidpour, M. Uysal, and M. Kavehrad, "BER performance of free-space optical transmission with spatial diversity," IEEE Transactions on Wirel. Commun. **6**, 2813–2819 (2007).
11. G. Yang, M. A. Khalighi, S. Bourennane, and Z. Ghassemlooy, "Fading correlation and analytical performance evaluation of the space-diversity free-space optical communications system," J. Opt. **16**, 035403 (2014).
12. G. T. Djordjevic, M. I. Petkovic, J. A. Anastasov, P. N. Ivanis, and Z. M. Marjanovic, "On the effects of correlation on outage performance of fso-unbalanced multibranch sc receiver," IEEE Photonics Technol. Lett. **28**, 1348–1351 (2016).
13. J. M. Garrido-Balsells, A. Jurado-Navas, J. F. Paris, M. Castillo-Vázquez, and A. Puerta-Notario, "Spatially correlated gamma-gamma scintillation in atmospheric optical channels," Opt. Express **22** (2014).
14. J. M. Garrido-Balsells, A. García-Zambrana, and A. Puerta-Notario, "Variable weight MPPM technique for rate-adaptive optical wireless communications," Electron. Lett. **42** (2006).
15. A. Jurado-Navas, J. M. Garrido-Balsells, M. Castillo-Vázquez, and A. Puerta-Notario, "Closed-form expressions for the lower-bound performance of variable weight multiple pulse-position modulation optical links through turbulent atmospheric channels," IET Commun. **6** (2012).
16. J. Garrido-Balsells, A. Jurado-Navas, J. F. Paris, M. Castillo-Vázquez, and A. Puerta-Notario, "Closed-form BER analysis of variable weight MPPM coding under gamma-gamma scintillation for atmospheric opti-

cal communications," Opt. Lett. **37**, 719–721 (2012).
17. V. Aalo, "Performance of maximal-ratio diversity systems in a correlated Nakagami-fading environment," IEEE Transactions on Commun. **43**, 2360–2369 (1995).
18. J. García-Fernández, A. Jurado-Navas, M. Fernández-Navarro, and C. Úbeda, "Efficient star-topology solving local minima for geolocation in real UMTS networks: an experimental assessment with real data," Wirel. Pers. Commun. **85**, 2115–2140 (2015).
19. A. Jurado-Navas, C. Úbeda, J. García-Fernández, and M. Fernández-Navarro, "Location of terminals in a communications network," (2019). US Patent Application No. 10257804 B2. Patent granted Apr. 9th, 2019.
20. L. Andrews, R. Phillips, C. Hopen, and M. Al-Habash, "Theory of optical scintillation," J. Opt. Soc. Am. A **16**, 1417–1429 (1999).
21. X. Zhu and J. Kahn, "Free-space optical communication through atmospheric turbulence channels," IEEE Transactions on Commun. **50**, 1293–1300 (2002).
22. V. Tatarskii, *The Effects of the Turbulent Atmosphere on Wave Propagation* (Keter, Jerusalem, 1971).
23. A. Jurado-Navas, A. García-Zambrana, and A. Puerta-Notario, "Efficient lognormal channel model for turbulent fso communications," Electron. Lett. **43**, 178–180 (2007).
24. A. Jurado-Navas and A. Puerta-Notario, "Generation of correlated scintillations on atmospheric optical communications," J. Opt. Commun. Netw. **1**, 452–462 (2009).
25. M. S. Alouini, A. Abdi, and M. Kaveh, "Sum of gamma variates and performance of wireless communication systems over nakagami-fading channels," IEEE Transactions on Veh. Technol. **50**, 1471–1480 (2001).
26. A. Oppenheim and R. W. Schafer, *Discrete-time Signal Processing* (Prentice Hall, 1999).
27. M. Al-Habash, L. Adrews, and R. Phillips, "Mathematical model for the irradiance probability density function of a laser beam propagating through turbulent media," Opt. Eng. **40**, 1554–1562 (2001).
28. M. A. Naboulsi and H. Sizun, "Fog attenuation prediction for optical and infrared waves," Opt. Eng. **43**, 319–329 (2004).
29. ITU-R Report F.2106 1, *Fixed service applications using free-space optical links* (2010).
30. L. C. Andrews and R. L. Phillips, *Laser beam propagation through random media* (SPIE, 2005).
31. http://functions.wolfram.com/.
32. A. M. Mathai and H. J. Haubold, *Special Functions for Applied Scientists* (Springer, 2008).
33. C. Fox, "The G and H functions as symmetrical Fourier kernels," Transactions Am. Math. Soc. **98** (1961).
34. C. Mukasa, "Stochastic modeling of wireless communications in a fading environment via Fox's H-function," Ph.D. thesis, Faculty of The College of Engineering and Computer Science. Florida Atlantic University (2017).
35. K. Zhang, Z. Song, and Y. L. Guan, "Simulation of Nakagami fading channels with arbitrary cross-correlation and fading parameters," IEEE Transactions on Wirel. Commun. **3**, 1463–1468 (2004).
36. L. E. Nelson, G. Zhang, M. Birk, C. Skolnick, R. Isaac, Y. Pan, C. Rasmussen, G. Pendock, and B. Mikkelsen, "A robust real-time 100g transceiver with soft-decision forward error correction [invited]," J. Opt. Commun. Netw. **4**, B131–B141 (2012).
37. J. C. Juarez, D. W. Young, J. E. Sluz, and L. B. Stotts, "High-sensitivity dpsk receiver for high-bandwidth free-space optical communication links," Opt. Express **19**, 10789–10796 (2011).
38. F. Fidler, M. Knapek, J. Horwath, and W. R. Leeb, "Optical communications for high-altitude platforms," IEEE J. Sel. Top. Quantum Electron. **16**, 1058–1070 (2010).
39. J. Wang, J. Liu, S. Li, Y. Zhao, J. Du, and L. Zhu, "Orbital angular momentum and beyond in free-space optical communications," Nanophotonics. **11**, 645–680 (2022).
40. A. Munkhbayar, H. Kishikawa, and N. Goto, "8-ary oam shift keying for fso link with atmospheric turbulence," in *OSA Advanced Photonics Congress (AP) 2019 (IPR, Networks, NOMA, SPPCom, PVLED),* (Optica Publishing Group, 2019), p. SpTh3E.6.
41. D.-N. Nguyen, S. Zvanovec, and Z. Ghassemlooy, "Mitigation of dispersion and turbulence in a hybrid optical fibre and free-space optics link using electronic equalisation," Optik. **196**, 163154 (2019).
42. J. Wang, C. Lu, S. Li, and Z. Xu, "100 m/500 mbps underwater optical wireless communication using an nrz-ook modulated 520 nm laser diode," Opt. Express **27**, 12171–12181 (2019).
43. ITU-T, "G.709, interfaces for the optical transport network (otn)," International Telecommunication Union, 2003.
44. "fSona Networks, http://www.fsona.com/index.php. Accessed: 2021-12-30," .
45. L. C. Andrews, R. L. Phillips, and C. Y. Hopen, "Aperture averaging of optical scintillations: power fluctuations and the temporal spectrum," Waves Random Media **10**, 53–70 (2000).
46. A. D. Wheelon, *Electromagnetic Scintillation: II. Weak Scattering* (Cambridge Univ. Press, New York, 2003).
47. G. I. Taylor, "The spectrum of turbulence," Proc. Royal Soc. Lond. Ser. A, Math. Phys. Sci. **164**, 476–490 (1938).
48. H. L. Dryden, G. B. Schubauer, W. C. Mock, and H. K. Skramstad, "Measurements of intensity and scale of wind-tunnel turbulence and their relation to the critical reynolds number of spheres," (1937). National Advisory Committee for Aeronautics, Tech. Report 581.
49. A. N. Kolmogorov, "The local structure of turbulence in incompressible viscous fluid for very large reynolds numbers," in *Proceedings of the USSR Academy of Sciences,* (1941), p. 299–303.
50. V. I. Tatarskii, *Wave Propagation in a Turbulent Medium* (McGraw-Hill, New York, 1961).
51. J. R. Dunphy and J. R. Kerr, "Scintillation measurements for large integrated-path turbulence∗," J. Opt. Soc. Am. **63**, 981–986 (1973).
52. M. E. Gracheva, A. S. Gurvich, S. S. Kashkarov, and V. V. Pokasov, "Similarity relations for strong fluctuations of light in a turbulent medium," Zh. Eksp. Teor. Fiz . 67, 2035–2046 (1974).[Sov. Phys. JETP 40, 1011–1016.
53. W. A. Coles and R. G. Frehlich, "Simultaneous measurements of angular scattering and intensity scintillation in the atmosphere," J. Opt. Soc. Am. **72**, 1042–1048 (1982).
54. B. J. Rickett, W. A. Coles, and G. Bourgois, "Slow scintillation in the interstellar medium," Astron. Astrophys. **134**, 390–395 (1984).
55. A. Prokhorov, F. Bunkin, K. Gochelashvily, and V. Shishov, "Laser irradiance propagation in turbulent media," Proc. IEEE **63**, 790–811 (1975).
56. J. Strohbehn, *Modern theories in the propagation of optical waves in a turbulent medium* (Springer Berlin Heidelberg, Berlin, Heidelberg, 1978), pp. 45–106.
57. A. Jurado-Navas, J. M. Garrido-Balsells, J. F. Paris, and A. Puerta-Notario, "A unifying statistical model for atmospheric optical scintillation," in *Numerical Simulations of Physical and Engineering Processes,* J. Awrejcewicz, ed. (IntechOpen, Rijeka, 2011), chap. 8, pp. 181–206.
58. J. M. Garrido-Balsells, A. Jurado-Navas, J. F. Paris, M. Castillo-Vazquez, and A. Puerta-Notario, "Novel formulation of the $\mathcal{M}$ model through the generalized-k distribution for atmospheric optical channels," Opt. Express **23**, 6345–6358 (2015).
59. Z. Chen, S. Yu, T. Wang, G. Wu, S. Wang, and W. Gu, "Channel correlation in aperture receiver diversity systems for free-space optical communication," J. Opt. **14**, 125710 (2012).
60. F. J. Lopez-Martinez, G. Gomez, and J. M. Garrido-Balsells, "Physical-layer security in free-space optical communications," IEEE Photonics J. **7**, 1–14 (2015).
61. J. M. Garrido-Balsells, F. J. Lopez-Martinez, M. Castillo-Vázquez, A. Jurado-Navas, and A. Puerta-Notario, "Performance analysis of fso communications under los blockage," Opt. Express **25**, 25278–25294 (2017).
62. A. K. Majumdar and J. C. Ricklin, *Free-Space Laser Communications: Principles and Advances* (Springer, 2010).
63. J. Ma, Y. Fu, L. Tan, S. Yu, and X. Xie, "Channel correlation of free space optical communication systems with receiver diversity in non-kolmogorov atmospheric turbulence," J. Mod. Opt. **65**, 1063–1071 (2018).